Control of ultrafast excitonic shift current induced THz emission efficiency of layered MoS₂ crystals

Neetesh Dhakar and Sunil Kumar*

Femtosecond Spectroscopy and Nonlinear Photonics Laboratory,
Department of Physics, Indian Institute of Technology Delhi, Hauz Khas, New Delhi 110016, India
*kumarsunil@physics.iitd.ac.in

Following the ultrafast photoexcitation of a semiconductor, it embodies competing dynamics among photocarriers, many-body transient states of highly energetic excitons, and electron-hole liquid. Here, we show that femtosecond optical pulse excitation induces transient excitonic shift current contributing to stronger THz emission from a single crystalline bulk MoS₂ at low temperatures. The control of dominating excitonic shift current is elucidated from excitation density dependent experiments at varying temperatures. A strong decrease in the excitonic contribution beyond a critical fluence of 150µJ/cm² is observed at a very low temperature of 20K. This behavior suggests the formation of a new quantum condensate, i.e., the electron-hole liquid, in the regime when the exciton density is overwhelmingly large that the average spacing between exciton pairs is comparable to the exciton radius. Furthermore, the exciton density dependent THz emission at varying temperatures is consistent with the Varshni model and the crystal Debye temperature of 260K.

The charge-neutral bound electron-hole pairs, namely, excitons in semiconductors are held together by the Coulombic force between them, where the exciton binding energy varies depending on the dielectric constant of the semiconductor and the effective mass of the carriers ^{1, 2}. In most semiconductors, the excitons are highly unstable at room temperature. In the van der Waal's layered transition metal dichalcogenides (TMDs), upon appropriate optical excitation, much long-lived and stable excitons are formed quickly as one lowers the bulk sample temperature from the room temperature value³⁻⁵. In fact, exciton binding energies in thin TMDs are reasonably high to have stable excitons even at room temperature. By means of ultrashort laser pulses, the formation and decay dynamics of the excitons can be studied. Molybdenum disulfide (MoS₂) is one of the most popular TMD material systems. By ultrafast optical excitation, the transition of the bulk MoS₂ from an exciton-rich state at the low excitation fluences to one at different stages of macroscopic transient states of the correlated electron-hole pairs, such as the electron-hole plasma and electron-hole liquid (EHL), depending on the excitation fluences used, are known to us to some extent through transient photoluminescence and transient absorption studies⁶⁻⁸.

An ultrafast photoexcitation of a semiconducting bulk MoS2 leads to the creation of various transient photocurrents in the materials, either directly by the generation and decay of the photoexcited carrier density and the excitons. A dynamic coherent exciton population, generated directly by ultrafast optical excitation, can contribute to the formation of transient photocurrent, namely, the exciton shift-current⁹⁻¹¹. Such induced photocurrents can lead to the emission of electromagnetic radiation from the material, that in the terahertz (THz) realm¹²⁻¹⁴, if photoexcited by femtosecond laser pulses. In MoS₂, an azimuth-dependent THz emission behavior has been associated to nonlinear optical contributions rather than just the induced transient photoconductivity due to real photocarriers^{12, 15}. For the above bandgap ultrafast photoexcitation, THz radiation emission from bulk MoS₂ was considered to be originating primarily due to the surface depletion field mediated transient photocurrent^{13, 16}. An emergence of excitonic shift current, for the case, when the exciton absorption is well separated from the conduction continuum and the ultrafast excitation is performed at low temperatures so as the thermal annihilation of excitons into free carriers is minimized¹⁷, it is possible to realize it contributing to the THz radiation emission. For example, the ultrafast laser-induced exciton shift current in cadmium sulfide was studied for free space THz generation was reported recently¹⁷. Hu et al.²¹, employed the ultrafast electron diffraction method to explore the many-body structural dynamics triggered by near-resonant excitation of lowenergy indirect excitons in MoS₂. It is anticipated that the exciton-rich semiconducting bulk MoS₂ crystal must also garner the above-mentioned transient charge and excitonic shift currents thereby making them relevant even at the THz frequencies over and above the well-tested other optoelectronic applications ¹⁸⁻²⁰.

In the current work, we have studied pulsed THz emission properties of bulk single-crystalline MoS₂. A continuous enhancement in the THz generation efficiency at low temperatures, an overall THz generation efficiency getting more than doubled when the crystal temperature lowers from room temperature to around 20 K, is observed. Supported by excitation density dependent measurements, the above behavior has been attributed to originating from an ultrafast excitonic shift current due to direct excitation of low-energy indirect excitons by broadband femtosecond laser pulses centered at 800 nm. The results have been analyzed to quantitatively extract other contributors to the THz emission, i.e., the optical rectification and surface depletion

field induced photocurrent along with the dominating excitonic shift current, the latter being stipulated by the just below direct bandgap but above the indirect bandgap photoexcitation of the crystal.

A schematic is shown in Fig. 1(a) depicting the photoexcitation of the MoS₂ crystal by femtosecond laser pulses of variable polarization and emission of THz pulses in the reflection geometry. Femtosecond laser pulses having pulse duration of ~35 fs, central wavelength (photon energy) $\lambda_p(E_p) = 800 \, nm$ (1.55 eV) and pulse repetition rate of 1 kHz were taken from a Ti:Sapphire regenerative amplifier for the ultrafast photoexcitation of the sample by a collimated beam (diameter of ~3 mm) as well as the detection of emitted THz pulses. The THz pulse detection for a specific polarization was achieved by using electro-optic sampling in a nonlinear crystal in our home-built setup²²⁻²⁴. The pump excitation fluence in the experiments was controlled by using various neutral density filters while the temperature (T) of the sample was varied by placing it inside a close cycle liquid helium optical cryostat.

For a fixed excitation polarization and fluence of ~120 μ J/cm², the amount of the generated THz radiation continuously increased as the sample temperature was lowered from the room temperature. At a few representative temperatures, the real-time variation of the electric field of the radiated THz pulses as obtained from these experiments is presented in Fig. 1(b). The peak-to-peak value, E_{THz}^{PP} , of the corresponding THz field as indicated in Fig. 1(b), is a good measure of the THz generation efficiency at the given conditions. Hence, the same has been used to plot the outcomes for the THz generation efficiency under the above conditions but in the entire range of the sample temperatures in Fig. 1(c).

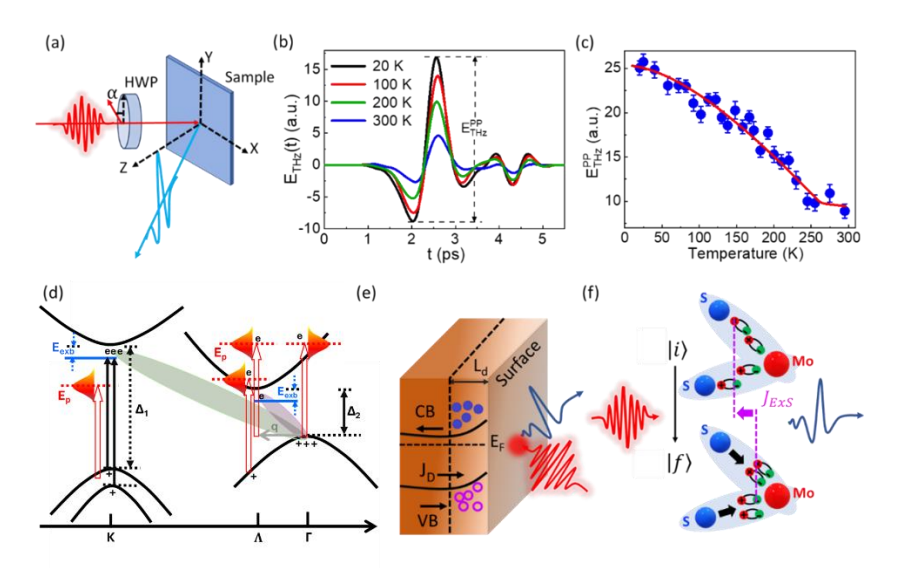


Figure 1. (a) Schematic for sample excitation by broadband femtosecond laser pulses of variable linear polarization and THz pulse emission in the reflection configuration. HWP: broadband zero-order half-wave plate at a variable angle α. (b) Typical THz pulses emitted from MoS₂ crystal shown for four temperatures, 300 K, 200 K, 100 K, and 20 K with a pump excitation fluence fixed at 120 $\mu J/cm^2$. The peak-to-peak value of the THz field, E_{THz}^{PP} is indicated. (c) Temperature dependence of E_{THz}^{PP} representing a monotonous increase in the THz generation efficiency with the decreasing temperature. The solid curve is fit to the data (see text). (d) Schematic electronic band-diagram and various transitions involving free carriers and excitons. Oval shapes indicate the Γ_v - K_c and Γ_v - Λ_c indirect excitons generated directly by the broadband femtosecond laser pulse excitation. Schematics for the THz pulse generation by (e) surface depletion field-mediated transient drift current J_D and (f) ultrafast exciton shift current J_{ExS} .

At low temperatures, MoS₂ is exciton-rich and hence those must contribute to THz emission for the observed temperature dependence in Fig. 1(c). A schematic electronic band-diagram is shown in Fig. 1(d) with Δ_1 = 1.85 eV and Δ_2 = 1.3 eV as the direct and indirect electronic bandgap energies at the K- and Γ -points, respectively, in the bulk MoS₂ crystal. Transitions involving free carriers and excitons as generated after the photoexcitation have also been indicated in the figure. As shown, at a given temperature, a phonon with momentum q participates in the free carrier photoexcitation across the bandgap Δ_2 at the zone-center point, Γ_v , between the valence band (VB) and the conduction band (CB) of the bulk MoS₂ crystal. Along with the direct excitons (E_A = 1.8 eV and E_B = 2 eV), and the exciton binding energy ($E_{exb} \sim 50$ meV), we have also included the Γ_v - K_c and Γ_v - Λ_c indirect excitons in the energy range of 1.33-1.59 eV and 1.23-1.44 eV, respectively^{21,25}, in the figure. The latter can be directly generated (indicated by oval shapes in the figure) by the broadband femtosecond excitation pulses used in the current experiments where the pump photon energy is just below the direct bandgap but above the indirect bandgap of the crystal. In the following, we describe the contributions of

a transient excitonic shift current J_{ExS} at low temperatures and transient drift photocurrent J_D due to photocarriers at room temperature towards the THz generation from MoS₂. We have utilized here a bulk MoS₂ crystal in 3R phase which lacks inversion symmetry³² and hence can exhibit the generation of an excitonic shift current.

The photogenerated excitons are less stable or short lived at room temperature due to the presence of active phonons and dissociate either to free carriers or annihilate by recombination. Hence, majorly, free carriers contribute to THz emission at high temperatures via the transient photocurrent effect (TPE) in which the photocarriers are accelerated under an internal electric field. This internal electric field can arise due to two reasons, i.e., the surface depletion field and the photo Dember field. The surface depletion field at the air-material interface of any semiconductor is like what is depicted in Fig. 1(e) under which the photocarriers drift causing a transient drift photocurrent J_D . It is given as $J_D = ne\mu E_s$, n being the photocarrier density, e the electronic charge, μ the carrier mobility and E_s the surface depletion field. For the Dember field to cause a photocurrent, the semiconductor necessitates to have a significant difference in the electron and hole mobilities. This is the reason for it to have been attributed in the THz emission from narrow bandgap semiconductors, such as InAs and InSb.²⁶ In bulk MoS₂, the electron and hole mobilities are quite comparable ²⁷, and hence THz emission due to the photo-Dember effect can be safely ignored. THz emission from other effects such as optical rectification (OR) and photon drag effect (PDE) also need to be considered. The latter, in which, photocarrier acceleration takes place due to direct transfer of incident photon momentum,28 THz emission for oblique incidence has been predominantly observed in materials possessing high concentrations of free carriers²⁹, such as metals, heavily doped semiconductors, graphene, etc. In bulk MoS₂, the intrinsic carrier concentration is low and in fact, the carrier mobilities are also quite low at all temperatures, at least by two orders of magnitude lower when compared with graphene, a case in which a significant effect is seen.³⁰ Therefore, THz emission by PDE can also be ignored in our case here. On the other hand, OR at the surface and the bulk of the noncentrosymmetric crystal is always present. It is considered to relatively weakly contribute to the THz emission across all temperatures.³¹

At low temperatures, the excitons in MoS₂ become much stable due to the limited involvement of phonons and help in forming an additional photocurrent, i.e., the exciton shift current J_{ExS} . Our observation that the overall THz emission from MoS₂ gets nearly doubled at low temperatures clearly signifies the role of the J_{ExS} . A possible mechanism of the transient J_{ExS} generation⁹ accompanying the usual exciton formation at below bandgap photoexcitation at low temperatures, is schematically shown in Fig. 1(f). The excitons transition between $|i\rangle$ and $|f\rangle$ states causing spatial shift towards the Mo atoms in real space is driven by the geometric Berry connection in the energy space.¹⁷

To analyze the complete temperature-dependence of the overall THz signal (Fig. 1(c)), we proposed an extended Varshni's model, comprising the contributions from the excitonic shift current, the TPE, and the OR effects, given as

$$E_{THz}^{PP}(T) = \left(E_{THz}^{PP}(0) - \frac{\alpha T^2}{(\beta + T)}\right) - \gamma T + \delta \tag{1}$$

Here, α , β , γ , and δ are real positive constants. The first term on the right-hand side (inside small brackets) is motivated from Varshni's model³³ for the exciton binding energy and hence accounts for the excitonic contribution. Here, $E_{THz}^{PP}(0)$ represents the maximum value of the THz radiation attainable from the J_{ExS} at the lowest temperature while, the constant β determines the Debye temperature of the system. The second term (γT) is for the contribution by TPE in which an increased scattering of the photocarriers with the increasing temperature reduces the carrier mobility³⁴ and hence the J_D^{23} . The constant δ accounts for near temperature-independent contribution to THz emission by $OR^{35,36}$. The sum of all three components, according to Eq. (1), is plotted in Fig. 1(c) where a good fit (solid curve) with the data validates the consistency of the model used here, particularly, the ultrafast excitonic shift current as derived from the Varshni's temperature-dependent exciton binding energy model. The fit yields $\beta \sim 260~K$, i.e., a value consistent with the Debye temperature³⁷ of the bulk MoS₂.

The excitation fluence (F) dependence of the E_{THZ}^{PP} was measured as shown in Fig. 2 for specific temperatures of 300 K, 200 K, and 150 K and in Fig. 3 for 20 K. These results also support our initial proposition that excitonic shift current is the major contributor to the THz emission at low temperatures. From Figs. 2 and 3, we note that except for the peculiar behavior at 20 K, a strong saturating behavior of the E_{THZ}^{PP} with the excitation fluence is present which makes it apparently clear that the THz radiation generation via OR is relatively much weaker. At 300 K, the amount of THz emission via TPE increases quickly with excitation fluence up until a saturation value F_S . Above F_S , the excessive photocarriers incoherently scatter from the phonons more than they can produce a coherent photocurrent J_D . At the lower temperature of 250 K, there is a substantial fraction of photogenerated excitons that constitute J_{EXS} and hence take part in the THz radiation generation concurrently with the photocarriers. As we lower the temperature further, the density of photogenerated excitons increases much rapidly with the increasing F and so is its contribution to the THz emission via coherent J_{EXS} . The saturation in the THz emission is attained much quicker at lower sample temperatures and the difference in the magnitudes is indicative of the role of the J_{EXS} .

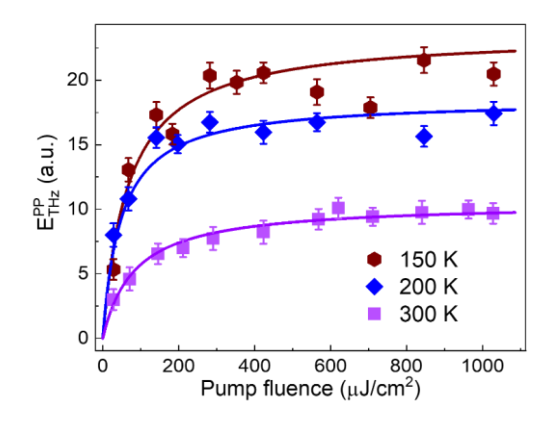


Figure 2. Photoexcitation fluence-dependent THz emission at various sample temperatures. The solid curves represent the model given in Eq. (2) for extracting the saturation fluence (F_s) .

We have used a phenomenological model given by 14

$$E_{THZ}^{PP} = S_1 F + S_2 \left[1 - \frac{1}{(1 + F/F_2)} \right] \tag{2}$$

 $E_{THZ}^{PP} = S_1 F + S_2 \left[1 - \frac{1}{(1+F/F_S)} \right]$ (2) to capture the saturating behavior of the E_{THZ}^{PP} with the excitation fluence F. Here, S_1 and S_2 are constant scaling factors. The first term of Eq. (2) quantifies the contribution to THz emission due to the nonlinear OR and J_{ExS} , while the second term shows the contribution of saturating J_D . The obtained values of F_s exhibit an increasing trend with the temperatures but they remain well below $120 \,\mu J/cm^2$.

As can be seen from Fig. 3, at the lowest temperature of 20 K, the exciton density and hence the amount of THz generation due to J_{ExS} rises rapidly with the increasing fluence. Beyond a critical excitation fluence $F_C \sim 150 \ \mu J/cm^2$, sudden drop in the E_{THz}^{PP} magnitude is seen which then attains a much lower and nearly constant value at higher fluences. A less prominent drop in the THz generation efficiency near the critical fluence is also evident from the result at 150 K (Fig. 2), where the stable exciton density is not significantly high and hence the excitonic shift current is not yet the dominant one toward THz emission. Above the critical fluence, the sudden drop in the THz emission due to dominating excitonic shift current at the low temperatures is indicative of a critical density of the photogenerated excitons at which the free exciton-rich state transitions to an electron-hole liquid condensate.

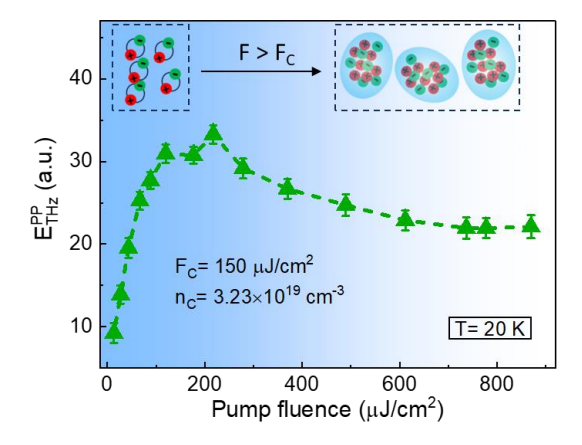


Figure 3. Photoexcitation fluence-dependent THz emission from bulk MoS2 at the lowest sample temperature of 20 K. Insect represents a rapid formation of excitons with the increasing fluence and transition to electron-hole liquid condensate beyond a critical excitation fluence $F_C \sim 150 \ \mu J/cm^2$.

Two regions of the excitation fluence, i.e., $F < F_C$, and $F > F_C$, are distinguished in Fig. 3. When $F < F_C$, the exciton density increases rapidly with the excitation fluence and hence an enhanced THz emission from the excitonic shift current follows up. At $F = F_C$, the exciton density is so high that the average spacing between pairs is nearly the same as the exciton radius. Therefore, the pairwise Coulomb interaction between electrons and holes of the excitons screens out for them to rather be dissociated into separate electrons and holes ensemble³⁸. This situation rather favors the formation of an electron-hole liquid condensate^{39, 40}. Moreover, at high fluences, bandgap renormalization⁷ causes a reduction in bandgap energy and the exciton binding energy. Hence, in the $F > F_C$ region, due to the reduced binding energy, the remaining excitons are also dissociated into charge carriers leading to formation of many body condensate, i.e., electron-hole liquid droplets^{39, 40}. Within the self-sustained and confined volume of this new macroscopic quantum state, the electrons and holes move independently from one another. The decrement in the THz emission by drop in exciton density above F_C persists until $F \sim 580 \, \mu J/cm^2$ at which the exciton density becomes nearly null and only the J_D contribute at its saturation limit as indicated in Fig. 3.

Not only does the critical density of excitons (n_C) corresponding to critical fluence but also a temperature lower than a certain critical temperature (T_C) has to be appropriate to favor the transition from free exciton-state to the correlated EHL state. From our data, we now estimate the values of n_C and T_C for the formation of the EHL macrostate. Since, the critical temperature is related to the exciton binding energy³⁸ E_{exb} as $k_B T_C < 0.1 E_{exb}$, where k_B is Boltzmann constant, using $E_{exb} \sim 50~meV$ for bulk MoS₂,⁵ we obtain $T_C < 60~K$. Considering the quasi-equilibrium condition for the excitons, the critical density of the excitons is related to the critical fluence by the relation, $\frac{38}{\tau_p E_p} = \frac{n_C}{\tau}$, where a is the absorption coefficient at excitation photon energy E_p , τ_p is the excitation pulse duration and τ is the stable exciton mean life-time. We obtain a value, $n_C \sim 3.2 \times 10^{19}~cm^{-3}$ for MoS₂ at $E_p = 1.55~eV$ and $F_C = 150~\mu J/cm^2$ as observed in our experiments. This value is very close to the Mott density in bulk MoS₂. Please see Section S6 for details.

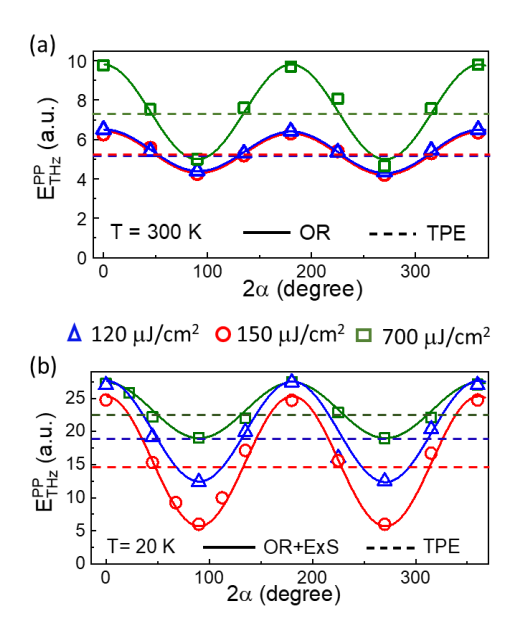


Figure 4. Variation of the emitted THz signal magnitude E_{THz}^{PP} with respect to the excitation polarization angle (α) obtained at (a) 300 K and (b) 20 K under different excitation fluence values of 120 $\mu J/cm^2$ ($F < F_C$), 150 $\mu J/cm^2$ ($F > F_C$).

Results obtained from the pump excitation pulse polarization angle (α) dependent experiments are summarized in Fig. 4 for the sample at the two extreme temperatures of 300 K and 20 K. These were taken at fixed values of the fluences, $F \sim F_C$ (150 $\mu J/cm^2$), $F < F_C$ and $F > F_C$. The experimental data in Fig. 4, represented by symbols, shows two-fold symmetric variation that is riding over a constant offset. This behavior can be well captured by the standard polarization-dependent model relation 14 , $E_{THZ}^{PP} = A\cos(2\alpha) + B$, as shown by solid lines. At 300 K temperature, the coefficients A and B are related to the OR and surface field-induced TPE contribution, while at 20 K, these coefficients are related to the OR+ExS and TPE processes, respectively. At 300 K, the contribution of the TPE process increases as the excitation fluence increases, specifically, at 700 $\mu J/cm^2$, the TPE process is more dominant than the OR effect. On the other hand, at 20 K temperature and at the critical pump fluence, polarization dependence is primarily due to the dominating excitonic shift current. These observations are consistent with the results presented earlier in the paper.

To summarize, we have investigated the excitonic shift current mediated THz emission from bulk MoS₂ upon photoexcitation by broadband femtosecond laser pulses centered at 800 nm. The experiments were carried out at varying temperatures, the excitation fluence, and the polarization, which helped us to extract the relative contribution of the excitonic shift current over the usual transient photocurrent towards the THz generation. Much importantly, at low temperatures where the excitons are the major contributor to the THz emission, we have observed a peculiar behavior in the fluence dependence of the THz emission, where the transition from free excitonic state to a correlated EHL macrostate can be attributed beyond a critical density of the excitons. Clearly,

by analyzing the THz emission from material systems, time-domain THz emission spectroscopy offers a novel tool for understanding photoinduced transitions noninvasively.

SK acknowledges the Science and Engineering Research Board (SERB), Department of Science and Technology, Government of India, for financial support through project no. CRG/2020/000892, and Joint Advanced Technology Center, IIT Delhi for support through EMDTERA#5 project. The authors thank Dr E Freysz for fruitful discussions and acknowledge financial support from CEFIPRA through project no. 6904-1. ND acknowledges CSIR for SRF.

REFERENCES

- Y. Lin, X. Ling, L. Yu, S. Huang, A. L. Hsu, Y.-H. Lee, J. Kong, M. S. Dresselhaus and T. Palacios, Nano Letters 14 (10), 5569-5576 (2014).
- 2. T. Mueller and E. Malic, npj 2D Materials and Applications 2 (1), 29 (2018).
- 3. Y. Jiang, S. Chen, W. Zheng, B. Zheng and A. Pan, Light: Science & Applications 10 (1), 72 (2021).
- 4. A. Arora, M. Koperski, K. Nogajewski, J. Marcus, C. Faugeras and M. Potemski, Nanoscale 7 (23), 10421-10429 (2015).
- 5. N. Saigal, V. Sugunakar and S. Ghosh, Applied Physics Letters 108 (13), 132105 (2016).
- Y. Park, S. W. Han, C. C. S. Chan, B. P. L. Reid, R. A. Taylor, N. Kim, Y. Jo, H. Im and K. S. Kim, Nanoscale 9 (30), 10647-10652 (2017).
- P. Dey, T. Dixit, V. Mishra, A. Sahoo, C. Vijayan and S. Krishnan, Advanced Optical Materials 11 (15), 2202567 (2023).
- 8. M. Karmakar, S. Mukherjee, S. K. Ray and P. K. Datta, Physical Review B 104 (7), 075446 (2021).
- 9. Y.-H. Chan, D. Y. Qiu, F. H. da Jornada and S. G. Louie, Proceedings of the National Academy of Sciences 118 (25), e1906938118 (2021).
- 10. R. Fei, L. Z. Tan and A. M. Rappe, Physical Review B 101 (4), 045104 (2020).
- 11. T. Morimoto and N. Nagaosa, Physical Review B 94 (3), 035117 (2016).
- 12. Y. Huang, L. Zhu, Q. Zhao, Y. Guo, Z. Ren, J. Bai and X. Xu, ACS Applied Materials & Interfaces 9 (5), 4956-4965 (2017).
- 13. I. Nevinskas, R. Norkus, A. Geižutis, L. Kulyuk, A. Miku, K. Sushkevich and A. Krotkus, Journal of Physics D: Applied Physics 54 (11), 115105 (2021).
- N. Dhakar, P. Zhao, H. Y. Lee, S.-W. Kim, B. Kumar and S. Kumar, ACS Applied Materials & Interfaces 16 (36), 47477-47485 (2024).
- Y. Huang, L. Zhu, Z. Yao, L. Zhang, C. He, Q. Zhao, J. Bai and X. Xu, The Journal of Physical Chemistry C 122 (1), 481-488 (2018).
- 16. N. Dhakar, S. Kumar, A. Nivedan and S. Kumar, Journal of Physics D: Applied Physics 56 (43), 435105 (2023).
- 17. M. Sotome, M. Nakamura, T. Morimoto, Y. Zhang, G. Y. Guo, M. Kawasaki, N. Nagaosa, Y. Tokura and N. Ogawa, Physical Review B 103 (24), L241111 (2021).
- 18. H. Lee, Y. B. Kim, J. W. Ryu, S. Kim, J. Bae, Y. Koo, D. Jang and K.-D. Park, Nano Convergence 10 (1), 57 (2023).
- 19. Y. Wu, Y. Wang, D. Bao, X. Deng, S. Zhang, L. Yu-chun, S. Ke, J. Liu, Y. Liu, Z. Wang, P. Ham, A. Hanna, J. Pan, X. Hu, Z. Li, J. Zhou and C. Wang, Light: Science & Applications 13 (1), 146 (2024).
- 20. D. Jariwala, V. K. Sangwan, L. J. Lauhon, T. J. Marks and M. C. Hersam, ACS Nano 8 (2), 1102-1120 (2014).
- 21. J. Hu, Y. Xiang, B. M. Ferrari, E. Scalise and G. M. Vanacore, Advanced Functional Materials 33 (19), 2206395 (2023).
- 22. S. Kumar and S. Kumar, Nature Communications 14 (1), 8185 (2023).
- 23. A. Nivedan and S. Kumar, New Journal of Physics 26 (3), 033044 (2024).
- 24. S. Kumar and S. Kumar, iScience 25 (8), 104718 (2022).
- 25. H.-P. Komsa and A. V. Krasheninnikov, Physical Review B 86 (24), 241201 (2012).
- 26. P. Gu, M. Tani, S. Kono, K. Sakai and X.-C. Zhang, Journal of Applied Physics 91 (9), 5533-5537 (2002).
- 27. S. Yu, H. D. Xiong, K. Eshun, H. Yuan and Q. Li, Applied Surface Science 325, 27-32 (2015).
- 28. Y. Huang, Z. Yao, C. He, L. Zhu, L. Zhang, J. Bai and X. Xu, Journal of Physics: Condensed Matter **31** (15), 153001 (2019).
- 29. P. Obraztsov, N. Kanda, K. Konishi, M. Kuwata-Gonokami, S. Garnov, A. Obraztsov and Y. Svirko, Physical Review B 90, 241416(R) (2014).
- 30. C.-H. Liu, Y.-C. Chang, S. Lee, Y. Zhang, Y. Zhang, T. B. Norris and Z. Zhong, Nano Letters 15 (6), 4234-4239 (2015).
- 31. D. Côté, N. Laman and H. M. van Driel, Applied Physics Letters 80 (6), 905-907 (2002).
- 32. J. Shi, P. Yu, F. Liu, P. He, R. Wang, L. Qin, J. Zhou, X. Li, J. Zhou, X. Sui, S. Zhang, Y. Zhang, Q. Zhang, T. C. Sum, X. Qiu, Z. Liu and X. Liu, Advanced Materials **29** (30), 1701486 (2017).
- 33. Y. P. Varshni, Physica 34 (1), 149-154 (1967).
- 34. K. Kaasbjerg, K. S. Thygesen and A.-P. Jauho, Physical Review B 87 (23), 235312 (2013).
- 35. S. Dahiya, S. Lahon and R. Sharma, Physica E: Low-dimensional Systems and Nanostructures 118, 113918 (2020).
- 36. A. R. Khan, B. Liu, L. Zhang, Y. Zhu, X. He, L. Zhang, T. Lü and Y. Lu, Advanced Optical Materials 8 (17), 2000441 (2020).
- 37. A. N. Gandi and U. Schwingenschlögl, Europhysics Letters 113 (3), 36002 (2016).
- 38. Y. Yu, A. W. Bataller, R. Younts, Y. Yu, G. Li, A. A. Puretzky, D. B. Geohegan, K. Gundogdu and L. Cao, ACS Nano 13 (9), 10351-10358 (2019).
- 39. W. F. Brinkman and T. M. Rice, Physical Review B 7 (4), 1508-1523 (1973).
- 40. G. Beni and T. M. Rice, Physical Review B 18 (2), 768-785 (1978).